

# Integrated fibres for self-monitored optical transport

MEHMET BAYINDIR<sup>1†</sup>, OFER SHAPIRA<sup>1,2</sup>, DURSEN SAYGIN-HINCZEWSKI<sup>3\*</sup>, JEFF VIENS<sup>3</sup>,  
AYMAN F. ABOURADDY<sup>1</sup>, JOHN D. JOANNOPOULOS<sup>1,4,5</sup> AND YOEL FINK<sup>1,3,4†</sup>

<sup>1</sup>Research Laboratory of Electronics, Massachusetts Institute of Technology, Cambridge, Massachusetts 02139, USA

<sup>2</sup>Department of Electrical Engineering and Computer Science, Massachusetts Institute of Technology, Cambridge, Massachusetts 02139, USA

<sup>3</sup>Department of Materials Science and Engineering, Massachusetts Institute of Technology, Cambridge, Massachusetts 02139, USA

<sup>4</sup>Center for Materials Science and Engineering, Massachusetts Institute of Technology, Cambridge, Massachusetts 02139, USA

<sup>5</sup>Department of Physics, Massachusetts Institute of Technology, Cambridge, Massachusetts 02139, USA

\*Permanent address: Department of Physics, Istanbul Technical University, Maslak 34469 Istanbul, Turkey

†e-mail: mehmet@mit.edu; yoel@mit.edu

Published online: 23 October 2005; doi:10.1038/nmat1512

**T**he ability to integrate distinct functional elements into a single device structure enables the realization of systems with higher-level functionality. Here we report on the design and fabrication of a fibre device structure that contains integrated optical, electrical and thermal elements for self-monitored optical transport. The fibre transmission element uses a hollow-core multilayer cylindrical photonic bandgap structure<sup>1,2</sup> designed to guide high-power radiation at 10.6  $\mu\text{m}$  along the fibre axis<sup>3</sup>. Multiple thermal-detection elements are placed in the vicinity of the hollow core for the purpose of temperature monitoring along the entire fibre length. Metal wires bridged by a semiconductor layer extend along the length of the fibre and deliver an electrical response to the fibre ends on change in the fibre temperature. The multimaterial fibre is drawn at high speeds from a single preform<sup>4</sup> to produce extended lengths of optically and thermally functional fibres. The exponential dependence on temperature of the electrical conductivity of the semiconducting material allows for the discrimination, in real time, between normal transmission conditions and those that are indicative of localized defect formation, thus enabling a self-monitoring high-power optical transmission line for failure prediction and prevention.

We report here on the design, fabrication and characterization of an integrated self-monitoring optical transport fibre for mid-infrared transmission. By combining four different materials, namely two amorphous chalcogenide semiconductors ( $\text{As}_2\text{Se}_3$  and  $\text{Ge}_{15}\text{As}_{25}\text{Se}_{15}\text{Te}_{45}$ ; GAST), a metal (Sn) and a polymer (polyethersulphone, PES), we prepared a macroscopic preform rod that shares the final fibre geometry. The preform was subsequently heated and drawn into functional fibres (see 'Preform preparation and fibre drawing' in Methods). Scanning electron microscopy micrographs (Jeol JSM-6060) of a representative fibre are shown in Fig. 1. This hybrid fibre has two functional components: (i) a hollow-core photonic bandgap (PBG) waveguide for  $\text{CO}_2$  laser transmission (Fig. 1a); and (ii) three metal–semiconductor–

metal (MSM) thermal detector elements for temperature sensing (Fig. 1b). Each element is an MSM device, with the two electrodes in Fig. 1b representing the metal contacts, and the 0.4- $\mu\text{m}$  thin GAST film extending between them is the semiconductor. Figure 1c and d reveals that the drawn fibre preserves the preform geometry during thermal cycling and elongation, which is a very challenging issue for composite material processing. Because of the large distance separating each device, their operation is rendered independent. Note that the three thermal-sensing devices are not operational at the preform level (because of the large distance between the electrodes) and they only become functional after drawing the fibre down to small dimensions.

The thermal detection layer described above is a tellurium-containing GAST thin film whose electrical conductivity is highly sensitive to temperature by virtue of the very small thermal activation energy. It is known that very stable glasses can be obtained with around 50% Te content<sup>5,6</sup>. We synthesized a quaternary glass in the Te-rich part of the glass-formation diagram (see 'Amorphous semiconductor synthesis' in Methods). The chosen glass composition was arrived at by optimizing the composition formula  $\text{Ge}_x\text{As}_{40-x}\text{Se}_y\text{Te}_{60-y}$  ( $10 < x < 20$  and  $10 < y < 15$ ) under constraints of compatibility of the glass-transition temperature and viscosity with the co-drawn polymer PES. This optimized glass further shows enhanced stability against crystallization during fibre drawing and high electrical responsivity to changes in temperature.

We start by characterizing the thermal-sensing elements of a 1,270- $\mu\text{m}$ -thick, 10-cm-long fibre by determining its resistance as a function of temperature. One of the thermal-sensing devices on the fibre was connected to an external circuit through its two metallic electrodes. The fibre was placed inside a hollow quartz tube, with the fibre's electrical connections still intact, and its temperature was raised by a resistive heater. The temperature inside the tube was measured by a thermocouple and the electrical current was simultaneously measured using a pico-ampere meter (Keithly 6487

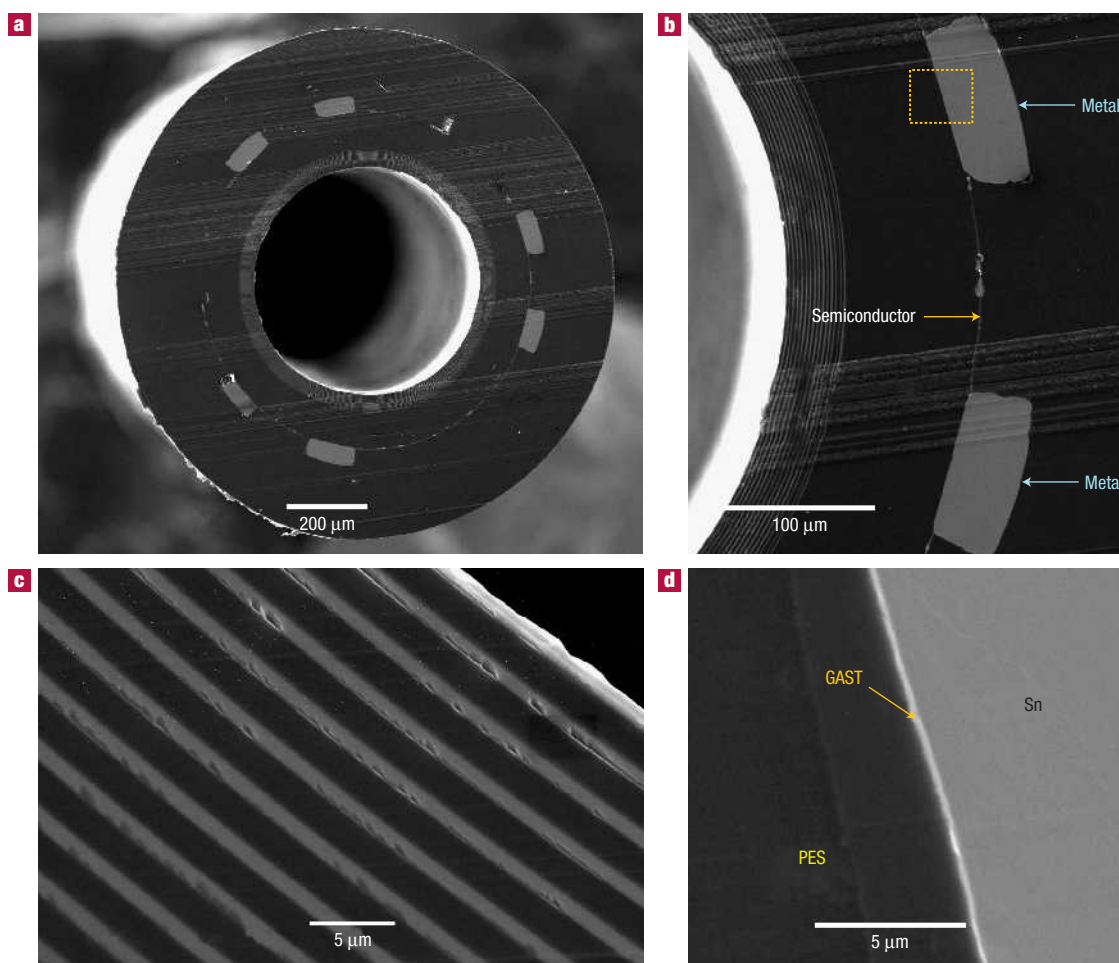


**Figure 1** Scanning electron micrographs of the hybrid fibre. **a**, The entire cross-section of the composite fibre, with 560  $\mu\text{m}$  hollow-core one-dimensional PBG structure, heat-sensitive layer, metallic conduits and protective polymer cladding. The outer diameter of the fibre is 1,270  $\mu\text{m}$ . **b**, The MSM heat sensor, which consists of a thin-amorphous-semiconductor (GAST) layer and two metal (Sn) electrodes. **c**, 13 pairs of alternating  $\text{As}_2\text{Se}_3$ /PES layers form a cylindrical mirror showing a PBG centred at 10.6  $\mu\text{m}$  for delivering a  $\text{CO}_2$  laser beam. **d**, A magnified micrograph of the box in **b** demonstrating the excellent quality of the insulator–semiconductor–metal interface.

picoammeter) with 50-V d.c. voltage applied. Figure 2a and b depicts both the temperature dependence of the fibre resistance and the current–voltage ( $I$ – $V$ ) characteristics of this MSM heat-sensing device. For amorphous semiconductors<sup>7</sup>, the resistivity can be expressed as  $\rho(T) \propto \exp(\Delta E/k_B T)$ , where  $\Delta E$  is the thermal activation energy,  $k_B$  is the Boltzmann constant and  $T$  is the absolute temperature. As shown in Fig. 2a, the measured resistivity of the GAST thin film as a function of temperature ranging from room temperature to 120 °C fits the above expression with  $\Delta E = 0.495$  eV. The  $I$ – $V$  curves in Fig. 2b indicate that the MSM junction has an ohmic behaviour at both low and high temperatures.

We now discuss the optical transport properties of the hybrid fibre. The fibre has a 560- $\mu\text{m}$ -diameter hollow core surrounded by a multilayer structure consisting of 13 bilayers of alternating  $\text{As}_2\text{Se}_3$  and PES having thicknesses of 1 and 1.9  $\mu\text{m}$ , respectively (Fig. 1c). The refractive indices of  $\text{As}_2\text{Se}_3$  and PES are 2.73 and 1.65 at 10.6  $\mu\text{m}$ , respectively (see <http://mit-pbg.mit.edu/Pages/DataBase.html> for spectroscopic ellipsometric data for these materials at near- and mid-infrared wavelengths). The calculated PBG diagram of the hybrid fibre is depicted in Fig. 2c. This structure results in an omnidirectional bandgap extending from 9.4 to 11.4  $\mu\text{m}$ . The blue

areas represent guided modes inside the core, whereas the red areas correspond to regions where light is not guided, but instead radiates through the multilayer structure. The inset in Fig. 2c shows a magnified segment of the PBG diagram detailing the guided modes near the light line ( $\theta = 90^\circ$ ), where the dispersion curves of three modes appear as light-blue stripes. The transmission spectrum of a 1-m-long fibre was measured by a Fourier-transform-infrared (FTIR) spectrometer (Tensor 37, Bruker) and is shown in Fig. 2d. Excellent agreement between the measured (Fig. 2d) and the calculated spectra (Fig. 2c) is observed.

Fibres used for infrared-laser-beam delivery<sup>3,8–12</sup>, regardless of the guiding mechanism or materials used, transport significant power densities through their core. Even a small defect nucleating within such a high-power optical transmission line can result in unintentional energy release with potentially catastrophic consequences. Heat generation in the cladding is predominantly because of either radiation leakage of the guided modes into the cladding or localized defect states. Typical radiation lengths range from a few metres for the low-order modes, to a few centimetres for higher-order modes. However, structural perturbations such as fibre bends and defects tend to increase the overall losses because of coupling to both higher-order propagating modes and to localized

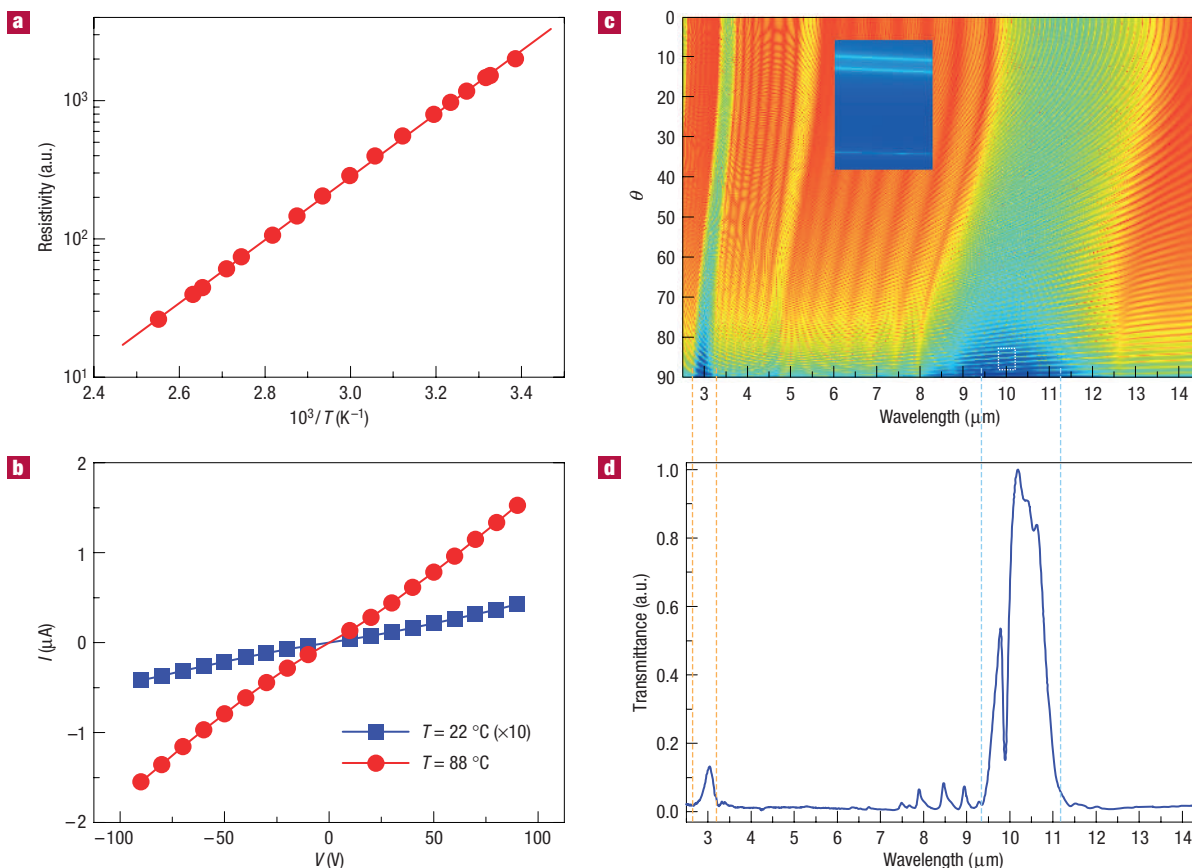


**Figure 2** Thermal, electrical and optical properties of the hybrid fibre. **a**, The measured resistivity of the GAST thin film in one of the devices in the fibre as a function of inverse temperature. The resistivity decreases more than two orders of magnitude when the temperature increases from room temperature to 120 °C. **b**, The  $I$ - $V$  characteristics of the heat sensor at low and high temperatures. The measured current at 22 °C was multiplied by a factor of ten in order to enhance visibility. **c**, The calculated band diagram of cylindrical multilayer PBG structure. The angle  $\theta$  is measured with respect to the normal to the fibre walls ( $\theta = 90^\circ$  coincides with the fibre axis). See text for details. **d**, The measured broadband transmission spectrum of the hollow-core PBG fibre. The primary and third-order gaps are centred at 10.6 and 3.0  $\mu\text{m}$ , respectively.

defect states. In such cases the radiated power from the multilayer structure is absorbed in the polymer cladding and transforms into heat. As a result, thermally excited electron-hole pairs in the GAST layer change its electrical conductivity. The equivalent conductance  $G_{\text{Eq}}$  of length  $L$  of the fibre can be modelled in terms of the local temperature distribution  $T(z)$  as  $G_{\text{Eq}} \propto \int_L \exp(-\Delta E/k_B T(z)) dz$ .

We demonstrate the delivery of high-power laser light through the hybrid fibre while monitoring the temperature in the fibre. A CO<sub>2</sub> laser (GEM-25, Coherent-DEOS) at 10.6  $\mu\text{m}$  was coupled to the fibre and a 50-V d.c. voltage was applied to the device electrodes. The input  $P_{\text{in}}$  and output  $P_{\text{out}}$  optical power, as well as the current through the electrodes, were recorded. We also measured the power radiated from the fibre outer surface and found it to be negligible with respect to the overall power loss. This suggests that the difference in power between the input and output dissipates in the fibre cladding and converts into heat, which was monitored further using an infrared camera (FLIR). We measured the fibre current as a function of the dissipated power  $\Delta P$  ( $\Delta P = P_{\text{in}} - P_{\text{out}}$ ) for a 40-cm-long bent fibre. We carried out several measurements for decreasing bend radii and recorded the output power, electrical current and temperature distribution (Fig. 3a) for a fixed input power of 2 W. The temperature distribution is found to have an oscillatory behaviour<sup>13</sup> because of mode beating between modes coupled by the bend<sup>14</sup>, with a gaussian envelope centred

midway on the fibre bend (Fig. 3b). As the mode-coupling strength is inversely proportional to the square of the bend radius<sup>15</sup>, an enhancement of the radiated power in the bend is expected, and consequently a rise in temperature. The results are presented in Fig. 3c, where the increase in current for higher dissipated power (lower bend radii) is easily observed. The equivalent resistance of the fibre was calculated assuming a gaussian function for  $T(z)$ . We found good agreement between the measured values and the calculated response as shown in Fig. 3c.

The potential use of this hybrid fibre to cope with the failure of waveguides in high-power laser systems by detecting faults before their occurrence is a very crucial achievement. Such failures are normally caused by distortions in the waveguide structure that result in the appearance of localized defect states. Consequently, high optical energy is coupled from the core to the defect state resulting in extensive heat generation. The ability to detect hot spots in the fibre can prevent catastrophic failures. However, the existence and location of defects are usually unknown *a priori*, and monitoring of the temperature along the fibre is required, as achieved by the temperature-sensing device embedded along the entire length of the fibre. The only challenge is to devise a method to obtain an indication of the local defect temperature from integrative current measurements, which we proceed to demonstrate. Earlier work on studying the temperature

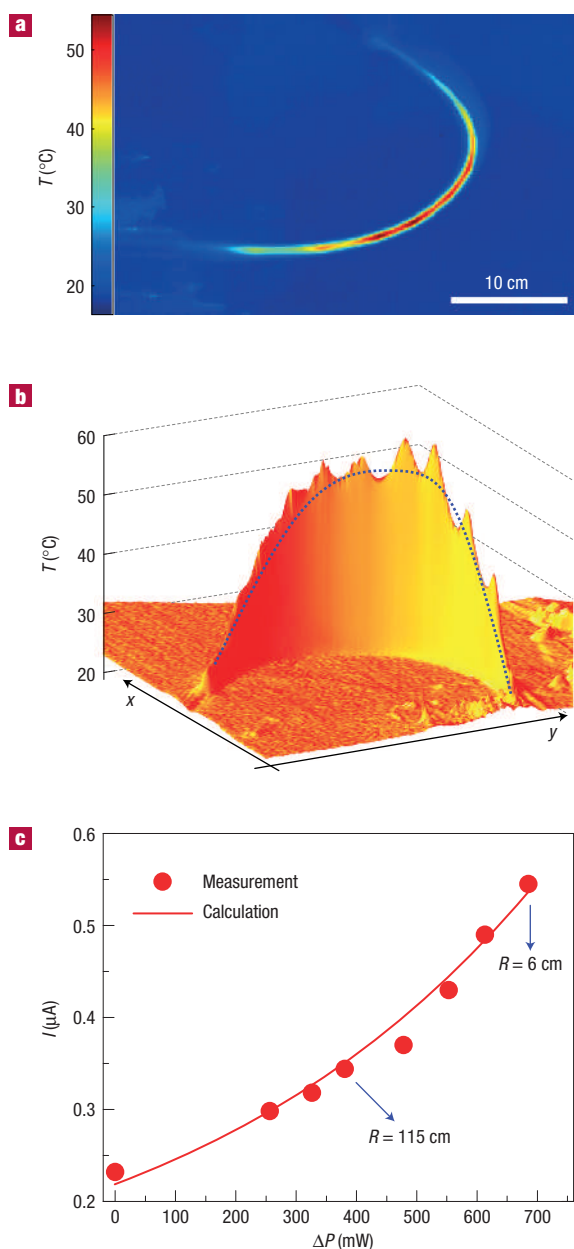


**Figure 3** Power dissipation along the bent fibre. **a**, A thermal photograph of a bent fibre captured by an infrared camera for a dissipated power of 700 mW. **b**, The temperature distribution along the fibre. Periodic variation in the temperature along the fibre is clearly seen. This is due to the fact that (orthogonal) modes are coupled by the fibre bend, resulting in mode beating. The  $x$  and  $y$  axes represent an arbitrary cartesian coordinate system in the plane of the fibre bend. **c**, The measured fibre current increases for decreasing bend radii for a fixed input laser power. The radii of curvature  $R$  range from the straight fibre case to  $R = 6$  cm. The dissipated power increases with decrease of  $R$  while maintaining  $P_{in}$  constant ( $\Delta P(R) = P_{in} - P_{out}(R)$ ). The theoretical model agrees well with the measurements.

distribution along fibres designed for high-power laser delivery have relied on scanning the external fibre surface using a point thermal sensor<sup>13,16</sup>. This approach obviates the possibility of real-time monitoring and is only feasible in a laboratory setting.

In order to investigate the self-fault-detection capabilities of our fibre, we measured the current as a function of the dissipated

power for defect-free and defective 40-cm-long fibres. The defect on the fibre was intentionally generated by burning a small spot on the fibre with a CO<sub>2</sub> laser beam. The temperature distributions along the fibres were recorded using an infrared camera for fixed dissipated power, as shown in Fig. 4a. Whereas the temperature is low and almost constant along the defect-free fibre, a high-temperature spot is observed at the location of the defect on the other fibre. These measured temperature profiles are fitted to gaussian distributions in Fig. 4b. The areas under the two curves are equal as expected, as the dissipated powers in both cases are equal. Thus, for fixed dissipated power (equal areas of the gaussian thermal distribution), defects that are more localized (narrower widths of the distributions) result in a higher peak temperature. A highly nonlinear relation exists between the temperature distribution and the measured current, which results in the capability of ascertaining whether a certain amount of power loss is attributed to a highly localized defect or a uniformly distributed loss. Because of this nonlinear relation, the currents generated in these two cases are not equal, even though the amount of dissipated optical power is equal.

The current recorded for these two fibres (by their respective sensitive elements) reveals a marked divergence as a function of dissipated power, as shown in Fig. 4c. The solid lines are calculated using the temperature data obtained by the infrared camera and then implementing the above-described model of fibre conductivity. Our model of the electrical response of the heat-sensing device indicates an exponential dependence of the local conductivity on temperature. This suggests that a point on the fibre having a temperature much higher than the rest would provide the dominant contribution to the current. In fact, for a given dissipated optical power, the current increases exponentially with increase in the peak temperature along the fibre. This significant difference between these fibres (defect-free and single-defect-containing) for identical dissipated powers clearly suggests that a sufficient condition for determining fibre failure from current measurements can be obtained, and a damage threshold current can hence be set. Note that the case of a bent fibre is intermediate between these two extremes, and the curve for current versus dissipated power (Fig. 3c) would lie between the two curves depicted in Fig. 4c.

To place a failure onset, we calculated the current as a function of maximum temperature along the fibre (which is inversely proportional to the temperature-distribution width, see Fig. 4b) for a dissipated power of 360 mW. The solid curve in Fig. 4d represents the results of this calculation. We also plot in Fig. 4d three experimental points corresponding to a defect-free straight fibre (blue circle), a defect-free bent fibre (green circle) and a single-defect-containing straight fibre (red circle). In the absence of a localized defect, the current does not exceed a certain threshold value for straight and bent configurations. Hence, when the monitored current exceeds a critical value (failure onset) for a fixed input power level, it is most likely to be caused by heat-generated defects on the inner surface of the fibre.

We have demonstrated the ability to integrate optical transport and fault monitoring for failure prediction, which is of paramount importance if high-power optical transmission lines are to be operated safely and reliably in medical<sup>17</sup>, industrial and defence applications. This work may also pave the way for different types of fibre-sensor device, such as thermal-sensing fabrics (M.B., A.F.A., J.D.J. and Y.F., manuscript in preparation).

## METHODS

### AMORPHOUS SEMICONDUCTOR SYNTHESIS

The bulk GAST glass rod, 10 mm in diameter and 15 cm in length, was prepared from high-purity (5–6N) Ge, As, Se and Te elements (Alfa Aesar) using conventional sealed-ampoule melt-quenching

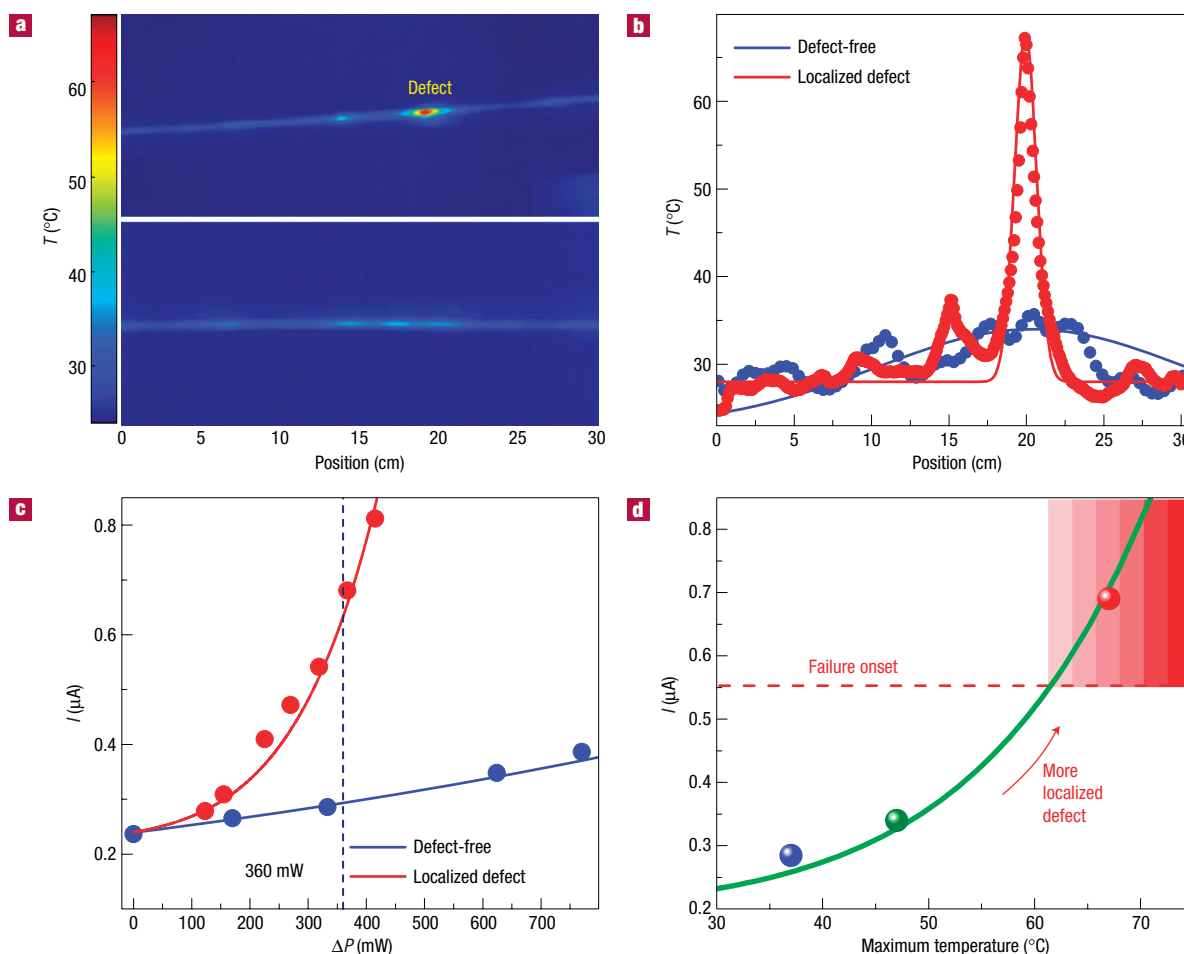


**Figure 4** High-power-laser-light delivery through the hybrid fibre and failure prediction. **a**, Thermal photographs of a fibre containing a single localized defect (upper panel) and a defect-free fibre (lower panel) captured by the infrared camera. Both fibres carry identical  $\text{CO}_2$  laser energy. High-power infrared light accumulates at the defect site, and consequently heats up the region around the defect. **b**, Temperature distributions taken along one-dimensional sections of **a** for the two fibres. The solid lines provide gaussian fits to the measured temperature profiles for both cases. **c**, Measured currents as a function of dissipated laser power for defect-free and single-defect-containing straight fibres. The solid lines are calculated by assuming that the temperature distribution along the fibre is gaussian as in **b**. The current increases markedly in the defective fibre case. **d**, The calculated current as a function of the maximum temperature along the fibre for a constant dissipated power. A higher maximum temperature corresponds to a more localized defect (a narrower temperature distribution at the defect site). See text for details.

techniques. The materials were weighed and placed into a quartz tube under a nitrogen atmosphere. The tube was heated to  $330^\circ\text{C}$  for 1 h at a rate of  $1^\circ\text{C min}^{-1}$  under vacuum in order to remove surface oxides. The ampoule was formed by sealing the tube under vacuum ( $\sim 10^{-5}$  torr). It was then heated to  $900^\circ\text{C}$  at a rate of  $2^\circ\text{C min}^{-1}$  in a rocking furnace for 18 h, while held vertical, and then rocked for 6 h to increase mixing and homogenization. The glass liquid was cooled to  $700^\circ\text{C}$  in the furnace and then quenched in cold water. Subsequently, it was annealed for 30 min near the glass-transition temperature,  $T_g = 190^\circ\text{C}$ , before being cooled gradually to room temperature. The  $10\text{-}\mu\text{m}$ -thick GAST film was deposited by thermal evaporation with a vacuum evaporator (Ladd Industries) on one side of a  $50\text{-}\mu\text{m}$ -thick PES film. The evaporation rate was kept below  $3\text{ nm s}^{-1}$  in order to obtain a stoichiometric deposition. The film was then annealed for 1 h at  $30^\circ\text{C}$  below the glass-transition temperature in a vacuum oven.

#### PREFORM PREPARATION AND FIBRE DRAWING

The macroscopic preform that shares the final fibre geometry was prepared by using the following steps. (i)  $\text{As}_2\text{Se}_3$ -coated PES film was rolled onto a  $14.2\text{-mm}$ -thick teflon FEP rod.  $13\text{-}\mu\text{m}$ -thick  $\text{As}_2\text{Se}_3$  films were uniformly deposited on either side of a  $50\text{-}\mu\text{m}$ -thick,  $24\text{-cm}$ -wide and  $1\text{-m}$ -long PES film by thermal evaporation with a custom-made vacuum evaporation system. (ii) After rolling a buffer PES layer with a thickness of a few millimetres, a single GAST layer was rolled. (iii) This heat-sensitive GAST layer was contacted by six Sn metal conduits ( $0.8\text{-mm}$  thick,  $2.5\text{-mm}$  wide and  $15\text{-cm}$  long) that were encapsulated in a protective PES cladding. (iv) A Teflon tape was rolled onto the outer surface of the preform in order to keep the PES layers tight before consolidation. (v) The preform was consolidated for 70 min at  $260^\circ\text{C}$  under vacuum ( $\sim 10^{-3}$  torr) in a three-zone horizontal-tube furnace while the preform was rotated about its axis. (vi) The Teflon rod was removed from the core immediately after consolidation. (vii) The preform was annealed for 1 h at  $180^\circ\text{C}$  in a vacuum oven and then cooled gradually to room temperature. The preform was heated and drawn into tens of metres of fibre in a draw tower (Heathway). Fibres were drawn at the central zone of a three-zone vertical-tube furnace (Thermcraft) with a top-zone temperature of  $190^\circ\text{C}$  and a middle-zone temperature of  $295^\circ\text{C}$ . The fibre diameter was monitored with laser-diameter monitors and the target fibre diameter was determined by measuring broad-band FTIR spectra during drawing.

Received 8 July 2005; accepted 16 September 2005; published 23 October 2005.

#### References

1. Yeh, P., Yariv, A. & Marom, E. Theory of Bragg fiber. *J. Opt. Soc. Am.* **68**, 1196–1201 (1978).
2. Fink, Y. *et al.* A dielectric omnidirectional reflector. *Science* **282**, 1679–1682 (1998).
3. Temelkuran, B., Hart, S. D., Benoit, G., Joannopoulos, J. D. & Fink, Y. Wavelength-scalable hollow optical fibres with large photonic bandgaps for  $\text{CO}_2$  laser transmission. *Nature* **420**, 650–653 (2002).
4. Bayindir, M. *et al.* Metal-insulator-semiconductor optoelectronic fibres. *Nature* **431**, 826–829 (2004).
5. Inagawa, I., Izuka, R., Yamagishi, T. & Yokota, R. Optical and thermal properties of chalcogenide Ge-As-Se-Te glasses for IR fibers. *J. Non-Cryst. Solids* **95–96**, 801–808 (1987).
6. Tikhomirov, V. K. *et al.* Glass formation in the Te-enriched part of the quaternary Ge-As-Se-Te system and its implication for mid-infrared optical fibres. *Infrared Phys. Technol.* **45**, 115–123 (2004).
7. Popescu, M. A. *Non-Crystalline Chalcogenides* (Kluwer Academic, Dordrecht, 2000).
8. Shephard, J. D. *et al.* High energy nanosecond laser pulses delivered single-mode through hollow-core PBG fibers. *Opt. Express* **12**, 717–723 (2004).
9. Harrington, J. A. *Infrared Fibers and Their Applications* (SPIE, Bellingham, Washington, 2004).
10. Abel, T., Hirsch, J. & Harrington, J. A. Hollow glass waveguides for broadband infrared transmission. *Opt. Lett.* **19**, 1034–1036 (1994).
11. Katagiri, T., Matsuura, Y. & Miyagi, M. Metal-covered photonic bandgap multilayer for infrared hollow waveguides. *Appl. Opt.* **41**, 7603–7606 (2002).
12. Dayan, A., Goren, A. & Gannot, I. Theoretical and experimental investigation of the thermal effects within body cavities during transendoscopic  $\text{CO}_2$  laser-based surgery. *Laser Surg. Med.* **35**, 18–27 (2004).
13. Karasawa, S., Miyagi, M. & Nishida, S. Temperature distribution along oversized hollow-core waveguides for infrared radiation. *Appl. Opt.* **26**, 4581–4586 (1987).
14. Johnson, S. G. *et al.* Low-loss asymptotically single-mode propagation in large-core omniguide fibers. *Opt. Express* **7**, 748–779 (2001).
15. Shapira, O., Abouraddy, A. F., Joannopoulos, J. D. & Fink, Y. Complete modal decomposition for optical waveguides. *Phys. Rev. Lett.* **94**, 143902 (2005).

16. Su, D., Somkuarnpanit, S., Hall, D. R. & Jones, J. D. C. Thermal effects in a hollow waveguide beam launch for CO<sub>2</sub> laser power delivery. *Appl. Opt.* **35**, 4787–4789 (1996).
17. Devaiah, A. K. *et al.* Surgical utility of a new carbon dioxide laser fiber: Functional and histological study. *Laryngoscope* **115**, 1463–1468 (2005).

#### Acknowledgements

We thank N. Orf for measuring the glass-transition temperature of the GAST glass. This work was supported in part by DARPA, the ARO, the ONR, the US DOE, and the ISN. This work was also

supported in part by the MRSEC Program of the National Science Foundation. D.S.H. was partly supported by the Istanbul Technical University president office grant. Correspondence and requests for materials should be addressed to M.B. or Y.F.

#### Competing financial interests

The authors declare that they have no competing financial interests.

Reprints and permission information is available online at <http://npg.nature.com/reprintsandpermissions/>